An Improved Duty-Cycle-Based Model Predictive Flux Control for Induction Motor Drives

Chenhui Zhou, Yongchang Zhang, *Fellow, IEEE*, Haitao Yang, *Member, IEEE*, and Wenyue Zheng

***Abstract*—Model predictive control with duty-cycle optimization has been widely adopted for induction motor drives. However, a fixed combination of a null vector and an active vector fails to guarantee the global optimal steady-state performance. Furthermore, the pulse pattern also has influence on the current harmonics and switching frequency, even if the same voltage vectors are applied. Aiming at solving these issues, an improved duty-cycle-based model predictive flux control is proposed in this paper. Firstly, the reference voltage vector is calculated by deadbeat flux control with space vector modulation (SVM), and then the optimal vector combination is obtained from SVM, which reduces the number of vector combination evaluations and enhance the steady state performance at high speeds by using two non-zero vectors. Secondly, to achieve minimum harmonic current and flux ripples, an optimal pulse pattern is employed, which places the active vector at the beginning and end of a vector sequence, and the middle vector may be a null vector or an active vector. Thirdly, the distribution ratio of the first vector is further optimized to minimize the flux ripple, leading to further performance improvement. Finally, the dynamic adjustment of vector sequences ensures a lower switching frequency. The experimental results confirm that the proposed control strategy has lower current THD than that of prior arts under similar switching frequency. The current THD can be reduced by nearly 60% at the rated speed with rated load.**

***Index Terms*—Duty cycle optimization, induction motor (IM), model predictive flux control (MPFC), symmetric vector sequence.**

I. Introduction

With the ever-increasing requirements in modern industrial production, the control of induction motors (IMs) is moving toward the center of stage [1]. The finite control set model predictive control (FCS-MPC) is actively developed in this process which gets rid of any external modulation stage to provide the optimized switching state [2]. Besides, FCS-MPC directly tracks the reference current or torque by enumerating the possible future states, making design and implementation more intuitive than those of the FOC and DTC methods [3]. Meanwhile, the flexible design of cost function ensures the reasonable management of various nonlinearities and multiobjective constraints [4].

However, it is worth-mentioned that weight coefficients are inevitable in the cost function of FCS-MPC as the number of control targets increases. Taking model predictive torque control (MPTC) as an example, the cost function consists of variables of different dimensions, namely, torque and stator flux. Thereby, MPTC suffers from the complicated tunning of weight coefficient. There is no systematic theory to realize the suitable selection of weight coefficients at present. To deal with this situation, model predictive flux control (MPFC) is proposed to avoid the need for a weighting factor by introducing the new stator flux vector to replace the original torque and stator flux in MPTC [5].

Through the enumeration and ranking, traditional MPC applies a single optimal voltage vector, which greatly limits the torque ripple and current harmonic performance of the system. By comparison, multiple-vector control applies multiple voltage vectors in one control cycle to achieve more precise error regulation [6], [7], [8].

Inspired by the improved DTC in [9], the concept of duty cycle optimization is introduced in FCS-MPC to enhance steady-state performance with simple control structure. In detail, the selected active voltage vector is only applied for a fraction of the control period and the remaining time is allocated for a null vector. In [10] and [11], one active vector and a null vector are selected to apply in one control period and the duration of the first vector is calculated via error minimization principles. When the second vector is not fixed as the null vector, the two applied voltage vectors are chosen relying on the premise that the duration time of each vector varies inversely as its cost function value. Thereby, the duration time of each vector in [12] and [13] are calculated by the cost function values, indicating that vector selection and duration optimization should be carried out simultaneously. Similarly, Zhang and Yang [14] calculated the duration of two active voltage vectors based on minimizing the flux error, while the optimizations of vector selection and duty ratio are processed in a cascaded fashion. However, multiple enumeration calculation and optimization increase the complexity of control. Many papers reduce the computational burden by reducing the number of candidate vectors and optimize the cost function. For example, in [15], a simplified cost function is built to evaluate

Received 1 January 2025; accepted 29 March 2025. Date of publication 8 April 2025; date of current version 30 June 2025. This work was supported in part by the Beijing Natural Science Foundation under Grant L247003 and in part by the Delta Power Electronics Science and Education Development Program of Delta Group. Recommended for publication by Associate Editor J. Hur. *(Corresponding author: Yongchang Zhang.)*

Chenhui Zhou and Yongchang Zhang are with the School of Electrical and Electronic Engineering, North China Electric Power University, Beijing 102206, China (e-mail: 120232101131@ncepu.edu.cn; yozhang@ieee.org).

Haitao Yang is with the Inverter Technologies Engineering Research Center of Beijing, North China University of Technology, Beijing 100144, China (e-mail: yhtao@ieee.org).

Wenyue Zheng is with the State Grid Jibei Electric Power Company Ltd., Tangshan Power Supply Company, Tangshan 063000, China (e-mail: zhengwy@ncepu.edu.cn).

Color versions of one or more figures in this article are available at https://doi.org/10.1109/TPEL.2025.3557914.

Digital Object Identifier 10.1109/TPEL.2025.3557914

the median line distance between space voltage vectors rather than the shortest distance, and the preselection of voltage vector with two steps is conceived to reduce the evaluation times. The duration of optimal voltage vectors in [16] are calculated using minimizing application of change in stator-flux, avoiding the repetitive computation of cost functions.

Alternatively, the idea of deadbeat control is adopted to select the optimal voltage vector faster which avoids the enumeration-based predictions [17], [18], [19]. In [17], the reference voltage vector, which nullifies the current error at the end of the next control period, is initially calculated. Subsequently, the best voltage vector is selected based on its minimal distance to the reference voltage vector. According to the principle of current deadbeat control, three adjacent voltage vectors and the corresponding duration in [20] and [21] are easily determined based on SVM, which reserves more computing space for subsequent vector selection and duty cycle adjustment. These methods contribute to simplified FCS-MPC strategies.

Regarding pulse patterns, the conventional dual-vector control methodology, which relies on duty cycle optimization, utilizes an asymmetric pulse arrangement where a nonzero vector precedes a zero vector within a control cycle. According to [22], this asymmetric pulse configuration leads to significant torque pulsations, prompting an attempt to organize symmetrical layouts by putting fixed null vectors on both sides of active voltage vectors. The quality of the current is indeed enhanced due to the reduction in the root mean square value of the ripple achieved through the adoption of a symmetrical pulse pattern. Considering that different instantaneous voltages will lead to different trajectories of current and flux linkage, thereby causing diverse current harmonics performance in different patterns, Li et al. [23] evaluated six possible symmetrical pulse arrangements regarding the current harmonics and switching frequencies. The optimal type of switching pulse is discovered at last where the active vectors are inserted on both sides of the vector sequence and the null vectors are chosen according to the active vector. Compared with the common pattern in [22], this pattern presents better current performance and lower switching frequency. Besides, while numerous studies have explored the utilization of two nonzero vectors within one control period to guarantee the optimal control performance in the full speed range [24], there still remains a lack of recognition that the advancement of symmetrical pulse mode can significantly enhance its steady-state performance to a greater extent.

Therefore, building upon the symmetric sequence pattern outlined in [23], this article broadens the synthesis scope of virtual voltage vectors, addressing the limitations associated with the conventional synthesis where the second vector is fixed as a zero vector. In addition, the vector duration is optimized, and the nonzero voltage vector in both sides of the vector sequence is no longer equally distributed. The main contributions are listed as follows.

1) The middle voltage vector can be possibly an active vector or a null vector rather than a null vector only in [23]. This is especially useful at high speeds with high modulation index [21]. However, in [21], it did not consider the symmetric pulse pattern, which applied the first voltage vector twice in the starting and ending of vector sequence.
2) Different from [23], which simply equals the vector duration of the first and the last voltage vector, the proposed method optimizes the vector duration of the first vector based on the principle of ripple minimization. This brings the benefits of lower steady state ripples.
3) The pulse pattern is dynamically adjusted based on the ending vector of the last vector sequence to achieve further switching frequency reduction. This achieves lower switching frequency with the same sampling frequency, which is beneficial to switching loss and system efficiency. Alternatively, the same switching frequency can be achieved with higher sampling frequency, which is beneficial to current total harmonic distortion (THD) reduction.

The rest of this article is organized as follows. The mathematical model of the whole drive system is described in Section II. The improved MPFC strategy is proposed in Section III, including the flux observer, duty-cycle optimization, and so on. In Section IV, the experimental results are described to show the effectiveness and superiority of the proposed strategy. Finally, Section V concludes this article.

II. System Description of a Two-Level Inverter-Fed IM

Considering that the rotor current cannot be measured directly, and speed is often regarded as a mechanical variable, the stator current and stator flux are chosen as state variables. In this way, a mathematical model of the IM can be constructed in a stationary frame as [25]

$$\frac{d\boldsymbol{x}}{dt} = \boldsymbol{A}\boldsymbol{x} + \boldsymbol{B}\boldsymbol{u} \tag{1}$$

$$\boldsymbol{y} = \boldsymbol{C}\boldsymbol{x} \tag{2}$$

with the coefficient matrices

$$\boldsymbol{A} = \begin{bmatrix} -\lambda(R_s L_r + R_r L_s) + j\omega_r & \lambda(R_r - jL_r\omega_r) \\ -R_s & 0 \end{bmatrix}$$

$$\boldsymbol{B} = \begin{bmatrix} \lambda L_r \\ 1 \end{bmatrix},\ \boldsymbol{C} = \begin{bmatrix} 1 & 0 \end{bmatrix},\ \lambda = \frac{1}{L_s L_r - L_m^2},$$

and the system variables $\boldsymbol{x} = \begin{bmatrix} \boldsymbol{i}_s & \boldsymbol{\psi}_s \end{bmatrix}^T$, $\boldsymbol{y} = [\boldsymbol{i}_s]$, $\boldsymbol{u} = [\boldsymbol{u}_s]$ where subscript s and r represent the stator information and rotor information, respectively; R, L, ω, $\boldsymbol{\psi}$, i, and u denote the resistance, inductance, electrical speed, flux vector, current vector, and voltage vector, respectively; L_m is the mutual inductance.

For a two level voltage source inverter, eight voltage vectors can be produced including two null voltage vectors and six active vectors, as shown in Fig. 1, where the whole plane is divided into six sectors and each sector contains two active voltage vectors and a null vector.

III. Principle of the Proposed MPFC

The whole control diagram of the proposed MPFC is presented in Fig. 2 and the details of each section are described as follows.

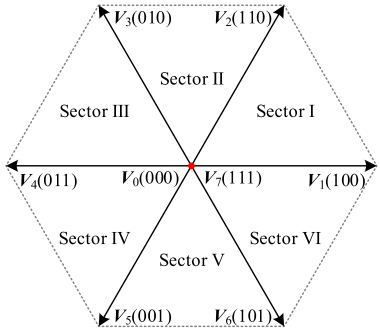

Fig. 1. Voltage vectors and sector division for two-level inverter.

A. Flux Observer

Accurate flux estimates are crucial for the high-performance control system of an IM. To ensure the accuracy of flux estimation over a wide speed range, the state observer can be utilized with stator current and flux chosen as the state variables [14]. In the two-phase stationary frame, the observer is built by state equation of IM as

$$p\hat{\boldsymbol{x}} = \boldsymbol{A}\hat{\boldsymbol{x}} + \boldsymbol{B}\boldsymbol{u}_s + \boldsymbol{G}\left(\boldsymbol{i}_s - \hat{\boldsymbol{i}}_s\right) \tag{3}$$

where $\hat{\boldsymbol{x}}$ is the estimated state variables, and $\hat{\boldsymbol{x}} = [\hat{\boldsymbol{i}}_s \quad \hat{\boldsymbol{\psi}}_s]$; G is the feedback gain matrix with the observer poles shifted to the left of IM poles, which is expressed as [26]

$$\boldsymbol{G} = -\begin{bmatrix} 2b \\ b/\left(\lambda L_r\right) \end{bmatrix} \tag{4}$$

where b denotes the distance moved to the left and $b<0$. In the following experimental tests, b is set as -40.

B. MPFC

In MPFC, the torque and flux should be predicted at (k+1)th instant to compensate for digital delay. To this end, the discretization of (1) is realized by Heun's method as shown in (5), which is able to obtain higher discrete accuracy than the first order Euler method [14]

$$\begin{cases} \boldsymbol{x}_p\left(k+1\right) & = \boldsymbol{x}(k) + T_{sc}\left(\boldsymbol{A}\boldsymbol{x}(k) + \boldsymbol{B}\boldsymbol{u}_s(k)\right) \\ \boldsymbol{x}\left(k+1\right) & = \boldsymbol{x}_p\left(k+1\right) + \frac{T_{sc}}{2}\boldsymbol{A}\left(\boldsymbol{x}_p\left(k+1\right) - \boldsymbol{x}(k)\right) \end{cases} \tag{5}$$

where $\boldsymbol{x}(k+1)$ is the predicted value of stator current and flux at (k+1)th instant, namely, $\boldsymbol{x}(k+1) = [\boldsymbol{i}_s(k+1) \quad \boldsymbol{\psi}_s(k+1)]^T$; $\boldsymbol{x}_p(k+1)$ is the corresponding correction of the predicted state variable; T_{sc} denotes the control period.

Thereafter, at (k+1)th instant, the rotor flux and torque can be further estimated respectively as

$$\boldsymbol{\psi}_r\left(k+1\right) = \frac{L_r}{L_m}\boldsymbol{\psi}_s\left(k+1\right) - \frac{1}{\lambda L_m}\boldsymbol{i}_s\left(k+1\right) \tag{6}$$

$$T_e\left(k+1\right) = 1.5N_p\lambda L_m\left(\boldsymbol{\psi}_r\left(k+1\right) \otimes \boldsymbol{\psi}_s\left(k+1\right)\right) \tag{7}$$

where N_p represents the pole pairs of IM and k+1 represents the information at (k+1)th instant.

If flux-weakening control and efficiency optimization are not considered, the amplitude of stator flux reference can be set as ψ_s^{ref}, that is

$$\mid \boldsymbol{\psi}_s^{\text{ref}} \mid = \psi_s^{\text{ref}}. \tag{8}$$

The reference of electromagnetic torque and stator flux can be expressed as (9) when the rotor flux has been obtained

$$T_e^{\text{ref}} = 1.5N_p\lambda L_m\left(\boldsymbol{\psi}_r \otimes \boldsymbol{\psi}_s^{\text{ref}}\right) \tag{9}$$

where $\boldsymbol{\psi}_r$ is obtained via the stator current and stator flux estimated according to (3).

To avoid complicated tuning work when cost function contains elements with different units and magnitudes, the stator flux vector is chosen as the control target since it is equivalently constructed from $T_e^{\text{ref}}$and ψ_s^{ref} based on the model of IM, which is expressed as

$$\angle\boldsymbol{\psi}_s^{\text{ref}} = \angle\boldsymbol{\psi}_r + \arcsin\left(\frac{T_e^{\text{ref}}}{1.5N_p\lambda L_m \mid \boldsymbol{\psi}_r \mid \psi_s^{\text{ref}}}\right) \tag{10}$$

$$\boldsymbol{\psi}_s^{\text{ref}} = \psi_s^{\text{ref}}\exp\left(j \cdot \angle\boldsymbol{\psi}_s^{\text{ref}}\right). \tag{11}$$

In digital implementation, there is typically a one-step delay between the selection of voltage vectors and their application. To compensate for this delay, it is necessary to predict the stator flux vector at the (k+2)th instant as (12). Consequently, the cost function can be expressed as (13)

$$\boldsymbol{\psi}_s\left(k+2\right) = \boldsymbol{\psi}_s\left(k+1\right) + T_{sc}\left(\boldsymbol{u}_s\left(k+1\right) - R_s\boldsymbol{i}_s\left(k+1\right)\right) \tag{12}$$

$$J = \mid \boldsymbol{\psi}_s^{ref} - \boldsymbol{\psi}_s\left(k+2\right) \mid. \tag{13}$$

C. Improved Pulse Pattern Selection

Most duty-cycle-based controls often arrange the symmetrical vector sequence to drive the system where the active voltage vector is in the middle and a zero vector $\boldsymbol{V}_0$ is distributed on both sides of the vector sequence. Nevertheless, by analyzing the variations of stator flux in different pulse patterns, Li et al. [23] discovered that the optimal pulse pattern is to arrange the null vector in the middle and distribute the active vector equally on both sides instead. In this way, the candidate voltage vectors for a control period are expanded from the original eight voltage vectors to any vector on the six blue lines as shown in Fig. 3. The applied vectors are viewed as the virtual vectors (VVs) synthesized by symmetric double vectors where the VVs in the direction of $\boldsymbol{V}_1$ are unified as $\boldsymbol{VV}_1$, and similarly in other directions. It is worth noting that the null vector inserted in the middle is determined by the three-phase minimum switching action. Thus, both current harmonics and switching losses can be suppressed. Taking $\boldsymbol{VV}_1$ and $\boldsymbol{VV}_2$ as examples, the specific pulse patterns are shown in Fig. 4. On this basis, this article further extends the candidate vector set to lay a foundation for better steady-state performance. Not only the synthesis of null and active vectors, but also the synthesis of two active vectors are considered as illustrated in red lines of Fig. 3. However, more candidate VVs undoubtedly aggravate the computational burden of the system.

To ensure a lower computational burden and control complexity at the same time, this article uses deadbeat control to

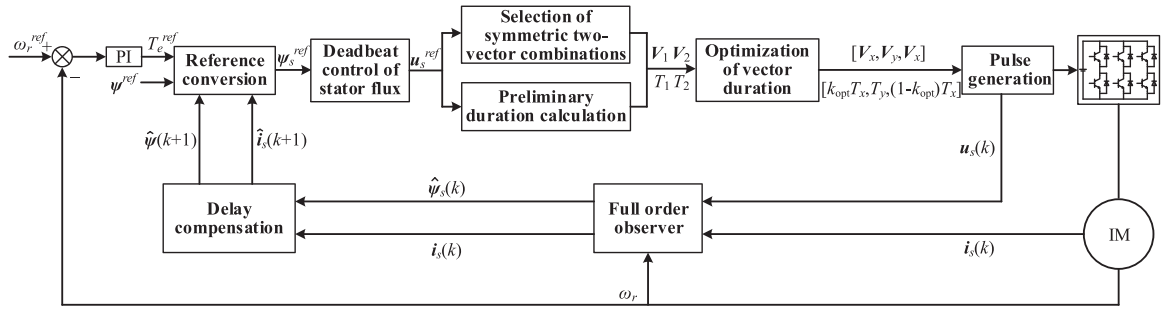

Fig. 2. Control diagram of the proposed strategy.

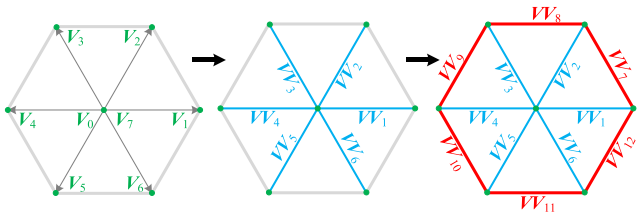

Fig. 3. Diagram of virtual voltage vectors' distribution.

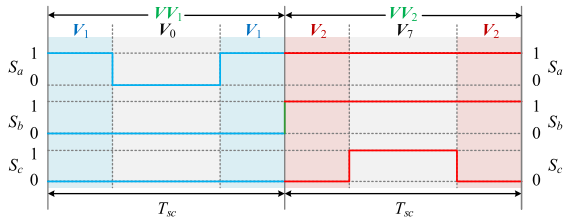

Fig. 4. Pulse pattern of two adjacent VVs in [23].

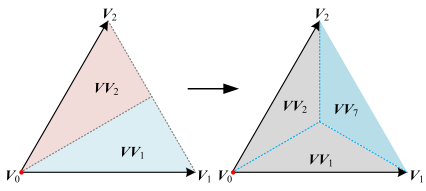

Fig. 5. Improved distribution of optimal vector in sector I.

obtain the duty-cycles conveniently. In theory, it is achieved when forcing the stator flux to reach its known reference at the end of next sampling period. By rebuilding (1), the reference of stator voltage can be deduced in the stationary frame as

$$\boldsymbol{u}_s^{\text{ref}} = R_s \boldsymbol{i}_s\left(k+1\right) + \frac{\boldsymbol{\psi}_s^{\text{ref}} - \boldsymbol{\psi}_s\left(k+1\right)}{T_{sc}}. \tag{14}$$

Then, the modulation index M and reference voltage angle θ to represent the amplitude and phase of $\boldsymbol{u}_s^{\text{ref}}$ are defined as follows:

$$\begin{cases} M = \dfrac{\sqrt{3}\|\boldsymbol{u}_s^{\text{ref}}\|}{U_{dc}} \\ \theta = \angle \boldsymbol{u}_s^{\text{ref}} \end{cases} \tag{15}$$

where U_{dc} represents the dc bus voltage.

In conventional SVM, the reference voltage is synthesized by two adjacent active vectors and null vectors. Taking the vectors in sector I as an example, $\boldsymbol{V}_1$, $\boldsymbol{V}_2$, $\boldsymbol{V}_0$, and $\boldsymbol{V}_7$ are considered to synthesize the applied vector. The corresponding duration can be calculated via the law of volt–second balance, as

$$\begin{cases} t_1 = M\sin\left(\frac{\pi}{3} - \theta\right) T_{sc} \\ t_2 = M\sin\left(\theta\right) T_{sc} \\ t_0 = T_{sc} - t_1 - t_2. \end{cases} \tag{16}$$

However, there are only two vectors for the final VV in the proposed MPFC. Therefore, the optimal voltage vectors should be decided after minimizing the cost function (13). Commonly, enumerations are used in predictions of MPFC, which incurs a heavy computational burden. By reducing the number of candidate vectors, the computational burden is naturally relieved.

The implied cost function of the proposed MPFC is built by subtracting (12) from (14) as

$$J' = \mid \boldsymbol{u}_s^{ref} - \boldsymbol{u}_s\left(k+1\right) \mid = \frac{1}{T_{sc}} \mid \boldsymbol{\psi}_s^{ref} - \boldsymbol{\psi}_s\left(k+2\right) \mid . \tag{17}$$

Obviously, it is proportional to the former cost function in (13). As a result, it is effective to choose the optimal vectors by the voltage error minimization. In this sense, when the reference voltage is located in the sector I, it is synthesized by $\boldsymbol{V}_1, \boldsymbol{V}_2, \boldsymbol{V}_0$ according to the deadbeat control. All candidate VVs are listed as $(\boldsymbol{V}_1, \boldsymbol{V}_0, \boldsymbol{V}_1)$, $(\boldsymbol{V}_0, \boldsymbol{V}_1, \boldsymbol{V}_0)$, $(\boldsymbol{V}_2, \boldsymbol{V}_7, \boldsymbol{V}_2)$, $(\boldsymbol{V}_7, \boldsymbol{V}_2, \boldsymbol{V}_7)$, $(\boldsymbol{V}_1, \boldsymbol{V}_2, \boldsymbol{V}_1)$, and $(\boldsymbol{V}_2, \boldsymbol{V}_1, \boldsymbol{V}_2)$ according to the principle of synthesizing symmetric vectors, as described previously.

In terms of $(\boldsymbol{V}_1, \boldsymbol{V}_2, \boldsymbol{V}_1)$, the final durations of $\boldsymbol{V}_1$, $\boldsymbol{V}_2$ are respectively devoted as $T_1 = t_1 + kt_0$ and $T_2 = t_2 + (1-k)t_0$, so that its corresponding volt–second error can be obtained as follows:

$$\left|\Delta \boldsymbol{V}_{121}\right|^2 = \left|\boldsymbol{V}_1 t_1 + \boldsymbol{V}_2 t_2 - \boldsymbol{V}_1 T_1 - \boldsymbol{V}_2 T_2\right|^2 \tag{18}$$

$$= t_0^2 \left|k\boldsymbol{V}_1 + (1-k)\boldsymbol{V}_2\right|^2 \tag{19}$$

$$= t_0^2 \left|\boldsymbol{V}_1\right|^2 \left(k^2 - k + 1\right) \tag{20}$$

where k is the allocation proportion for the duration of redundant null vector. It is evident that the minimum volt-second error is obtained at $k = 0.5$. The optimal pulse arrangement is the combination with the longest duration of candidate vectors, which can be specifically expressed as

$$V_{\text{opt}} = \text{argmin} \mid J' \mid = \text{argmax} \mid t_{\boldsymbol{u}1} + t_{\boldsymbol{u}2} \mid \tag{21}$$

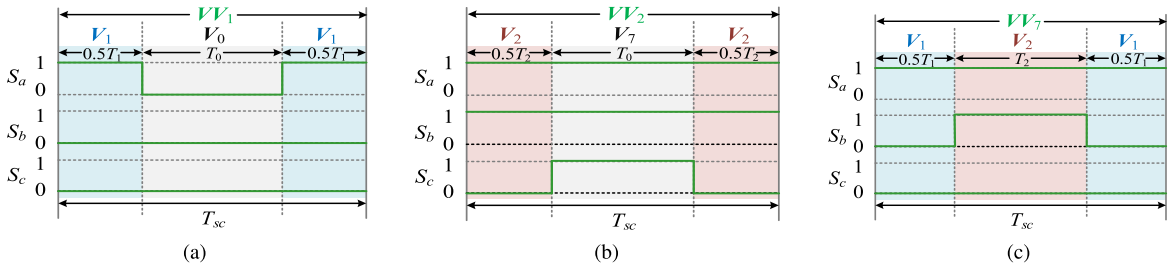

Fig. 6. Pulse patterns in sector I for (a) $t_2<\min(t_0,t_1)$, (b) $t_1<\min(t_0,t_2)$, and (c) $t_0<\min(t_1,t_2)$.

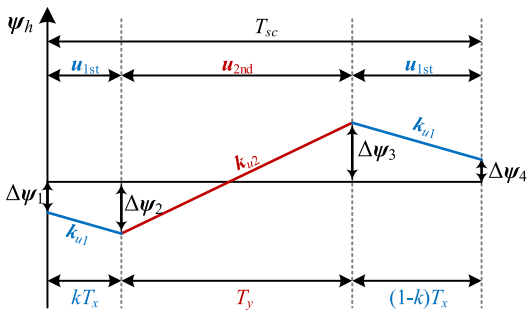

Fig. 7. Schematic of flux ripples for one control cycle.

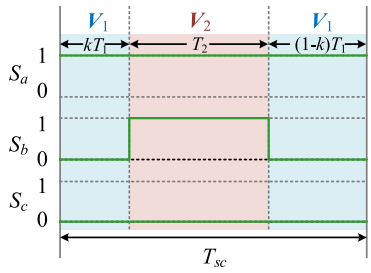

Fig. 8. Improved pulse pattern when $t_0<\min(t_1,t_2)$.

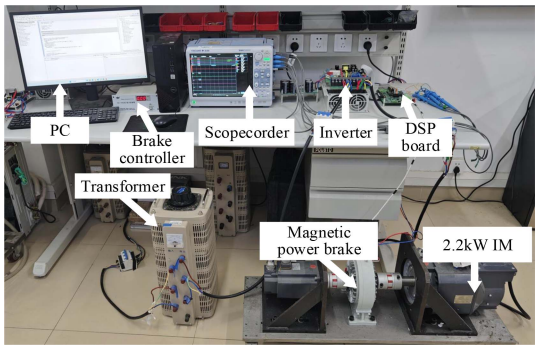

Fig. 9. Experimental setup of two-level inverter-fed IM drive.

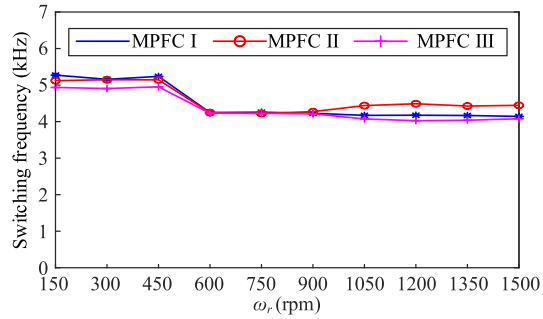

Fig. 10. Average switching frequencies for MPFC I, MPFC II, and MPFC III at different speeds with rated load.

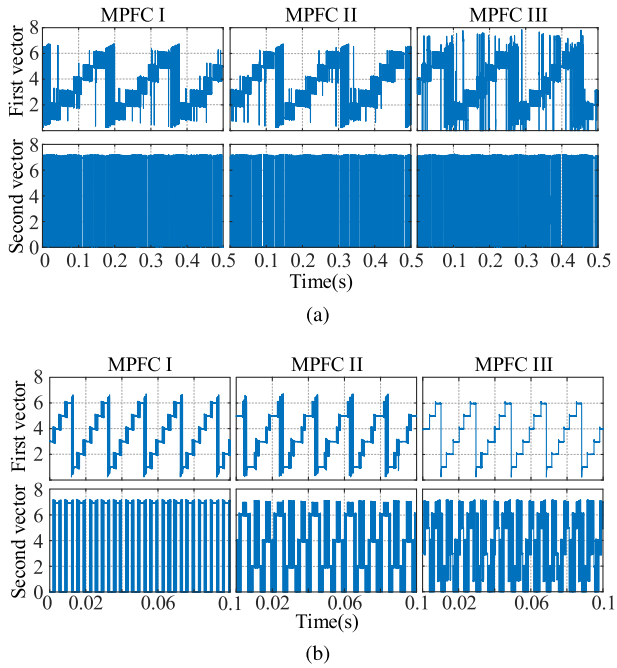

Fig. 11. Selected two vectors for MPFC I, MPFC II and MPFC III at (a) 150 rpm and (b) 1500 rpm.

where t_{u1} and t_{u2} are durations of any voltage vectors, such as u_1 and u_2.

Consequently, compared with the strategy in [23], the optimal vector arrangements of sector I can be chosen from the expanded candidate VVs as illustrated in Fig. 5, rather than the fixed VV_1 or VV_2. There are three possible pulse combinations in sector I, as shown in Fig. 6, while in the traditional method [23], only the first two pulse patterns are considered for the first sector.

D. Optimization of Vector Durations

It can be observed from Fig. 6 that the duration of the voltage vector in the symmetric vector set is completely equal at both

sides. However, this is based on previous experience in [23], and there is no guarantee that equal proportional distribution is optimal. Generally, the impact of the stator resistance can be ignored, so that the flux ripples in one PWM period can be obtained as

$$\boldsymbol{\psi}_h(t) = \int_{t_o}^{t_o+t} \left(\boldsymbol{u}_s^{\text{ref}} - \boldsymbol{u}(t)\right) dt \tag{22}$$

where $u(t)$ represents the discrete output voltages, and t_o denotes the start time of the control cycle. The difference between the output voltage and the reference voltage can be viewed as a constant in each section, so the flux ripples in a control period are a three-section polyline.

The RMS value of the flux ripples in a single PWM period can be expressed as

$$\boldsymbol{\psi}_h^{\text{rms}}(t) = \sqrt{\frac{1}{T_{sc}} \int_{t_o}^{t_o+T_{sc}} |\, \boldsymbol{\psi}_h(t)\,|^2\, dt}. \tag{23}$$

In order to avoid complicated integration operation, the rms value of the flux ripples are calculated by adding the values corresponding to the three independent lines. The root-mean-square value of a straight-line function is calculated as

$$L^{\text{rms}} = \sqrt{\frac{l_1^2 + l_1 l_2 + l_2^2}{3}} \tag{24}$$

where l_1 and l_2 represent the starting and ending values of the line function, respectively. Consequently, it is necessary to obtain flux ripples at different time points in a single PWM period. Actually, the flux ripples of the initial and final values of the linear function are

$$\begin{cases} \Delta\boldsymbol{\psi}_1 = \boldsymbol{\psi}_s^{\text{ref}}(k+1) - \boldsymbol{\psi}_s(k+1) \\ \Delta\boldsymbol{\psi}_4 = \boldsymbol{\psi}_s^{\text{ref}}(k+2) - \boldsymbol{\psi}_s(k+2). \end{cases} \tag{25}$$

Then, the middle value of flux ripples in such a linear function can be ensured by the (25) and the slope of the flux ripples in (26), as

$$\begin{cases} \boldsymbol{k}_{u1} = \dfrac{\boldsymbol{\psi}_s^{\text{ref}}(k+2) - \boldsymbol{\psi}_s^{\text{ref}}(k+1)}{T_{sc}} - (\boldsymbol{u}_{1\text{st}} - R_s \boldsymbol{i}_s(k+1)) \\ \boldsymbol{k}_{u2} = \dfrac{\boldsymbol{\psi}_s^{\text{ref}}(k+2) - \boldsymbol{\psi}_s^{\text{ref}}(k+1)}{T_{sc}} - (\boldsymbol{u}_{2\text{nd}} - R_s \boldsymbol{i}_s(k+1)) \end{cases} \tag{26}$$

$$\begin{cases} \Delta\boldsymbol{\psi}_2 = \Delta\boldsymbol{\psi}_1 + \boldsymbol{k}_{u1} \cdot kT_x \\ \Delta\boldsymbol{\psi}_3 = \Delta\boldsymbol{\psi}_2 + \boldsymbol{k}_{u2} \cdot T_y \end{cases} \tag{27}$$

where $\boldsymbol{u}_{1\text{st}}$ and $\boldsymbol{u}_{2\text{nd}}$ represent the first applied voltage vector and the second vector, T_x and T_y are durations of corresponding vectors, respectively. The flux ripples produced by different voltage vectors are presented in Fig. 7. Aiming at the minimum flux ripples, the optimal distribution ratio k_{opt} can be obtained as (28) shown at the bottom of this page, by solving $\partial \boldsymbol{\psi}_h^{\text{rms},2}/\partial k = 0$

TABLE I
OPTIMAL VECTOR SEQUENCES AND CORRESPONDING DURATIONS

Conditions	Optimal sequences	Optimal durations
t_0<min(t_1,t_2)	($\boldsymbol{V}_1$,$\boldsymbol{V}_2$,$\boldsymbol{V}_1$)	(kT_1,T_2,$(1-k)\,T_1$)
	($\boldsymbol{V}_2$,$\boldsymbol{V}_1$,$\boldsymbol{V}_2$)	(kT_2,T_1,$(1-k)\,T_2$)
t_1<min(t_0,t_2)	($\boldsymbol{V}_2$,$\boldsymbol{V}_7$,$\boldsymbol{V}_2$)	(kT_2,T_7,$(1-k)\,T_2$)
	($\boldsymbol{V}_7$,$\boldsymbol{V}_2$,$\boldsymbol{V}_7$)	(kT_7,T_2,$(1-k)\,T_7$)
t_2<min(t_0,t_1)	($\boldsymbol{V}_1$,$\boldsymbol{V}_0$,$\boldsymbol{V}_1$)	(kT_1,T_0,$(1-k)\,T_1$)
	($\boldsymbol{V}_0$,$\boldsymbol{V}_1$,$\boldsymbol{V}_0$)	(kT_0,T_1,$(1-k)\,T_0$)

TABLE II
VECTOR SEQUENCES OF VVS

Virtual vectors	Candidate vector sequences
$\boldsymbol{VV}_1$	($\boldsymbol{V}_1$,$\boldsymbol{V}_0$,$\boldsymbol{V}_1$),($\boldsymbol{V}_0$,$\boldsymbol{V}_1$,$\boldsymbol{V}_0$)
$\boldsymbol{VV}_2$	($\boldsymbol{V}_2$,$\boldsymbol{V}_7$,$\boldsymbol{V}_2$),($\boldsymbol{V}_7$,$\boldsymbol{V}_2$,$\boldsymbol{V}_7$)
$\boldsymbol{VV}_3$	($\boldsymbol{V}_3$,$\boldsymbol{V}_0$,$\boldsymbol{V}_3$),($\boldsymbol{V}_0$,$\boldsymbol{V}_3$,$\boldsymbol{V}_0$)
$\boldsymbol{VV}_4$	($\boldsymbol{V}_4$,$\boldsymbol{V}_7$,$\boldsymbol{V}_4$),($\boldsymbol{V}_7$,$\boldsymbol{V}_4$,$\boldsymbol{V}_7$)
$\boldsymbol{VV}_5$	($\boldsymbol{V}_5$,$\boldsymbol{V}_0$,$\boldsymbol{V}_5$),($\boldsymbol{V}_0$,$\boldsymbol{V}_5$,$\boldsymbol{V}_0$)
$\boldsymbol{VV}_6$	($\boldsymbol{V}_6$,$\boldsymbol{V}_7$,$\boldsymbol{V}_6$),($\boldsymbol{V}_7$,$\boldsymbol{V}_6$,$\boldsymbol{V}_7$)
$\boldsymbol{VV}_7$	($\boldsymbol{V}_1$,$\boldsymbol{V}_2$,$\boldsymbol{V}_1$),($\boldsymbol{V}_2$,$\boldsymbol{V}_1$,$\boldsymbol{V}_2$)
$\boldsymbol{VV}_8$	($\boldsymbol{V}_2$,$\boldsymbol{V}_3$,$\boldsymbol{V}_2$),($\boldsymbol{V}_3$,$\boldsymbol{V}_2$,$\boldsymbol{V}_3$)
$\boldsymbol{VV}_9$	($\boldsymbol{V}_3$,$\boldsymbol{V}_4$,$\boldsymbol{V}_3$),($\boldsymbol{V}_4$,$\boldsymbol{V}_3$,$\boldsymbol{V}_4$)
$\boldsymbol{VV}_{10}$	($\boldsymbol{V}_4$,$\boldsymbol{V}_5$,$\boldsymbol{V}_4$),($\boldsymbol{V}_5$,$\boldsymbol{V}_4$,$\boldsymbol{V}_5$)
$\boldsymbol{VV}_{11}$	($\boldsymbol{V}_5$,$\boldsymbol{V}_6$,$\boldsymbol{V}_5$),($\boldsymbol{V}_6$,$\boldsymbol{V}_5$,$\boldsymbol{V}_6$)
$\boldsymbol{VV}_{12}$	($\boldsymbol{V}_6$,$\boldsymbol{V}_1$,$\boldsymbol{V}_6$),($\boldsymbol{V}_1$,$\boldsymbol{V}_6$,$\boldsymbol{V}_1$)

Taking $(\boldsymbol{V}_1, \boldsymbol{V}_2, \boldsymbol{V}_1)$ as an instance, the pulse waveform can be corrected from Figs. 6(c) to 8. In general, through the flux ripples of one control cycle, the optimal duration of the symmetric two voltage vectors can be calculated online to obtain better steady-state performance. The optimal pulse arrangements in sector I are summarized in Table I.

E. Dynamic Adjustment of Vector Sequences

For the sake of lower switching frequency, the vector sequences are adjusted flexibly online in a control period with the principle of the least number of switching transitions. To be precise, if the optimal vector combination chosen by Table I is $(\boldsymbol{V}_1, \boldsymbol{V}_2, \boldsymbol{V}_1)$ and the last applied vector is $\boldsymbol{V}_3$, the vector sequences will be adjusted to $(\boldsymbol{V}_2, \boldsymbol{V}_1, \boldsymbol{V}_2)$ to produce fewer switching actions. It should be noted that after dynamic adjustment of vector sequence, there will be only one candidate voltage vector sequence as shown in Table II, which is subsequently substituted to (28) to calculate the optimal vector duration.

IV. EXPERIMENTAL TESTS

To highlight the advantages of the proposed MPFC, a series of comparative experiments are conducted on an IM drive fed

$$k_{\text{opt}} = \frac{\begin{array}{c}\Delta\boldsymbol{\psi}_1 \odot (2\Delta\boldsymbol{\psi}_1 - \Delta\boldsymbol{\psi}_4 + 2T_x\boldsymbol{k}_{u1} + 6T_y\boldsymbol{k}_{u1} - 2T_y\boldsymbol{k}_{u2}) \\ +\Delta\boldsymbol{\psi}_4 \odot (-\Delta\boldsymbol{\psi}_4 + T_x\boldsymbol{k}_{u1} - T_y\boldsymbol{k}_{u2}) + \boldsymbol{k}_{u2} \odot \left(3T_y^2\boldsymbol{k}_{u1} - T_y^2\boldsymbol{k}_{u2} + 2T_xT_y\boldsymbol{k}_{u1}\right)\end{array}}{-2T_x\boldsymbol{k}_{u1} \odot (\Delta\boldsymbol{\psi}_1 - \Delta\boldsymbol{\psi}_4 + \boldsymbol{k}_{u1}T_x + 3T_y\boldsymbol{k}_{u1} - 2T_x\boldsymbol{k}_{u2})}. \tag{28}$$

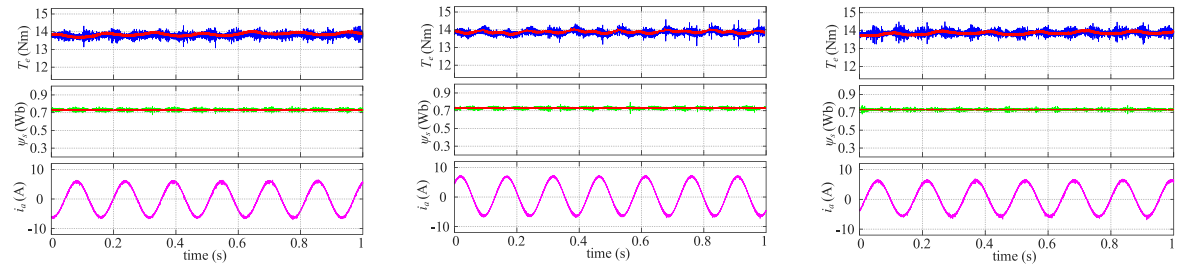

Fig. 12. Steady-state performance of 150 rpm with rated load for (a) MPFC I, (b) MPFC II, and (c) MPFC III.

TABLE III
PARAMETERS OF TESTED IMS

Rated power	P_N	2.2 kW
Dc-bus voltage	$U_{\rm dc}$	540 V
Rated voltage	U_N	380 V
Rated frequency	f_N	50 Hz
Number of pole pairs	N_p	2
Stator resistance	R_s	3.36 Ω
Rotor resistance	R_r	1.17 Ω
Mutual inductance	L_m	0.14 H
Stator inductance	L_s	0.15 H
Rotor inductance	L_r	0.15 H

by a two-level voltage source inverter, as presented in Fig. 9. The system and machine parameters are listed in Table III. The method proposed in [23] is called MPFC I, where the control variable is changed from current to flux. The proposed method without and with optimization of vector sequence and durations are referred to as MPFC II and MPFC III, respectively. The results obtained from traditional deadbeat control based on SVM (DBC-SVM) are also presented for the aim of comparison. The control algorithms are executed on a 32-bit floating DSP TMS320F28388 from TI [27]. All internal variables are acquired through the onboard DAC and plotted in MATLAB for the aim of analysis, while the stator current is directly measured using a current probe connected to a ScopeCoder DL950.

A. Steady-State Performance Comparison of Different MPFCs

To achieve a fair comparison, the average switching frequencies of three control strategies should be as close as possible. The sampling frequency of MPFC I and MPFC II is 10 kHz. For MPFC III, the sampling frequency is set to 11 kHz and the average switching frequency is shown in Fig. 10, where three MPFCs maintain similar switching frequencies in the whole speed range and the MPFC III always has slightly lower switching frequency.

In order to verify the satisfactory steady-state performance, the tests are carried out at different speeds with a rated load. At low speeds, the reference voltage vector has a very low amplitude, typically located in regions VV_1 and VV_2 of each sector in Fig. 5. Consequently, the optimal combination at these speeds involves a nonzero vector and a zero vector. This is further confirmed by the experimental results shown in Fig. 11(a), where the selected first vector and second vector are almost the same for the MPFC I and the proposed MPFC II. In MPFC III, the dynamic adjustment strategy of vector sequence is applied to reduce the switching frequency, so the application order of zero vector and nonzero vector is different.

The torque, stator flux, and phase current comparison at 150 rpm is illustrated in Fig. 12. All control methods demonstrate minor fluctuations, maintaining accurate speed tracking. The torque ripples for all three strategies remain below 0.8 Nm. The sinusoidal stator current exhibits satisfactory performance, with the THD of the current measured at 3.17%, 3.24%, and 3.39%, respectively. It is observed that the current THD of MPFC I is marginally lower compared to MPFC III, which can be attributed to its slightly higher switching frequency. Overall, at low speeds, the proposed MPFC III demonstrates similar and comparable performance to MPFC I.

At high speeds, the reference voltage vector is much larger due to the high back EMF caused by the high speed and it falls to region VV_7 in Fig. 5 frequently. As a result, the optimal combinations of MPFC II and MPFC III at high speeds include two nonzero vectors, which is confirmed by the selected voltage vectors at 100% rated speed shown in Fig. 11(b). Although both utilize nonzero vectors, it can be observed that the optimal vectors for MPFC II and MPFC III are distinct, primarily due to the application of online automatic vector adjustment technology in the latter. On the contrary, MPFC I still selects one null vector and an active voltage vector. Hence, it produces increased current harmonics and torque ripple at high speeds. Specifically, Fig. 13 shows the steady-state waveforms of three strategies at rated speed of 1500 rpm. The current THD of MPFC III is 4.46%, lower than the value of 12.02% in MPFC I and 4.88% in MPFC II, as presented in Fig. 14. The MPFC I has seriously increased torque and flux ripple at high speeds and is no longer able to track speed command accurately. The proposed control strategies still maintain very small torque ripples and flux ripples.

For evaluating the steady-state performance more comprehensively, a comparison at various command speed is exhibited in terms of current THD, torque ripple and stator flux ripple in Fig. 15. Obviously, the proposed MPFC III has the lowest current harmonics and torque ripple when the speed is above 300 rpm (20% rated speed). This advantage is more pronounced when the speed is above 1200 rpm (80% rated speed).

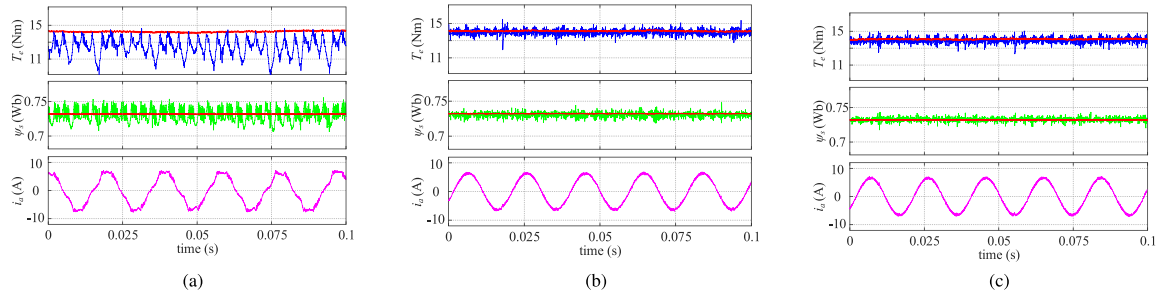

Fig. 13. Steady-state performance of 1500 rpm with rated load for (a) MPFC I, (b) MPFC II, and (c) MPFC III.

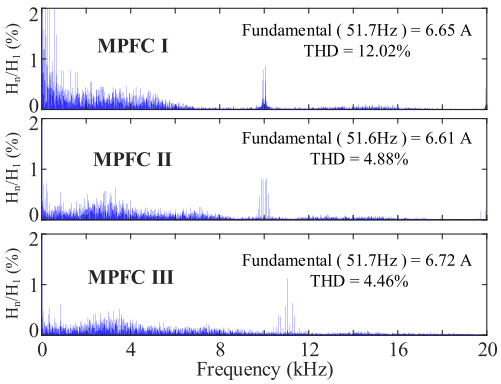

Fig. 14. Harmonic spectrum of stator current for MPFC I, MPFC II, and MPFC III at 1500 rpm.

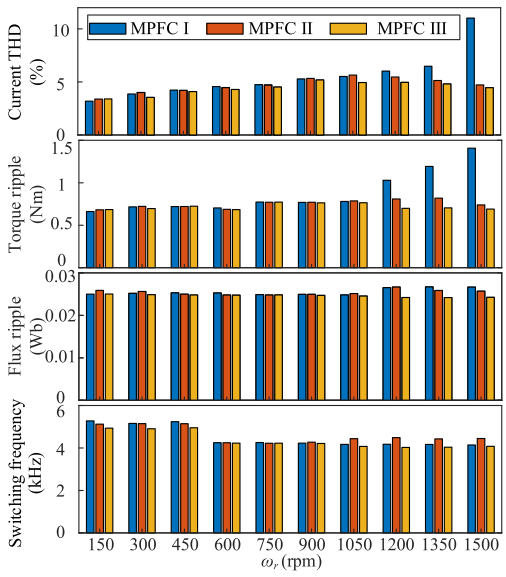

Fig. 15. Steady-state performance comparison of each method at various speeds in terms of current THD, torque ripple, and stator flux ripple.

Besides, this work adopts an insightful performance coefficient proposed in [28]. The scalar coefficient quantifies the product of the current THD and switching frequency, defined as

$$c_f = I_{\text{THD}} \cdot f_{\text{sw}} \tag{29}$$

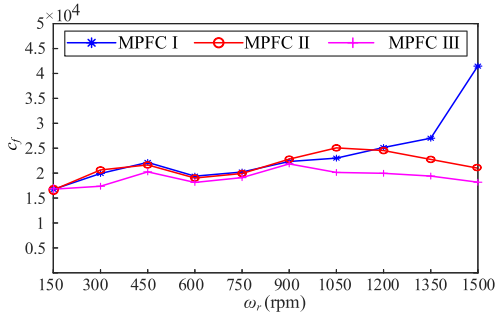

Fig. 16. Experimental results of performance coefficients under different speed commands with the rated load.

where c_f is the scalar performance coefficient, I_{THD} is the value of current THD, and f_{sw} is the inverter switching frequency. The results are based on varied speed command with constant load torque. As the c_f is lower, the performance is better. As observed in Fig. 16, MPFC III is the best one by presenting the lowest c_f over the entire speed range, especially when the speed is above 900 rpm. The performance of MPFC I and II are similar to each other when the speed is below 900 rpm. However, MPFC II performs better than MPFC I when the speed is above 1200 rpm. The results clearly show the effectiveness of optimization of vector order and vector duration in MPFC III when both switching frequency and current harmonics are concerned.

B. Steady-State Performance Comparison With DBC-SVM

To further confirm the effectiveness of the proposed method, the experimental comparison of the proposed MFPC III and DBC-SVM under the condition of similar switching frequency is carried out. The sampling frequency and switching frequency of DBC-SVM are 5 kHz. For MPFC III, the sampling frequency is set to 13 kHz and the average switching frequency is slightly lower than 5 kHz. Fig. 17(a) shows the steady-state waveforms of DBC-SVM and MPFC III at high-speed of 1500 rpm with rated load. It is seen that there are more ripples in the rotor speed, torque and stator current of DBC-SVM than those in MFPC III. The current THD of the MFPC III is 3.94%, which is reduced by 18.7% compared to the value of 4.83% in DBC-SVM, as shown in Fig. 17(b). The experimental results

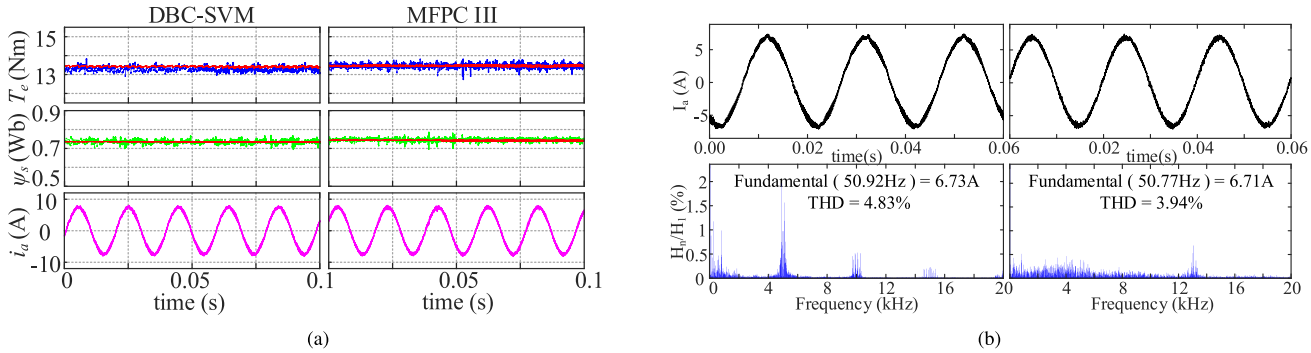

Fig. 17. Steady-state performance comparison at 1500 rpm between DBC-SVM and MFPC III (a) torque, stator flux, and current, (b) current THD.

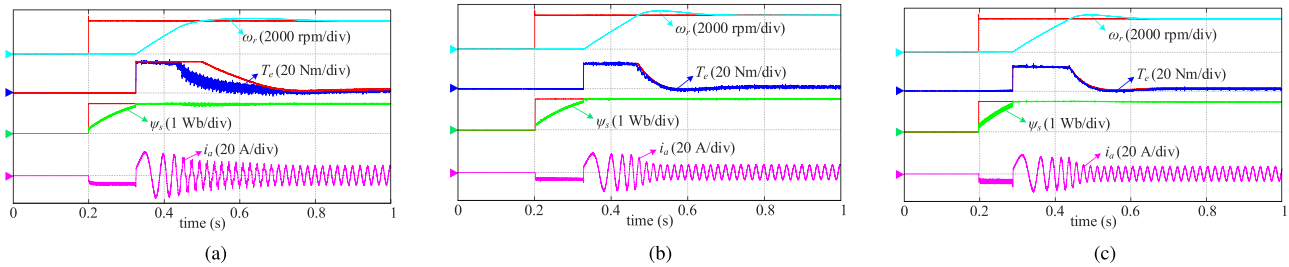

Fig. 18. Starting from standstill to 1500 rpm for (a) MPFC I, (b) MPFC II, and (c) MPFC III.

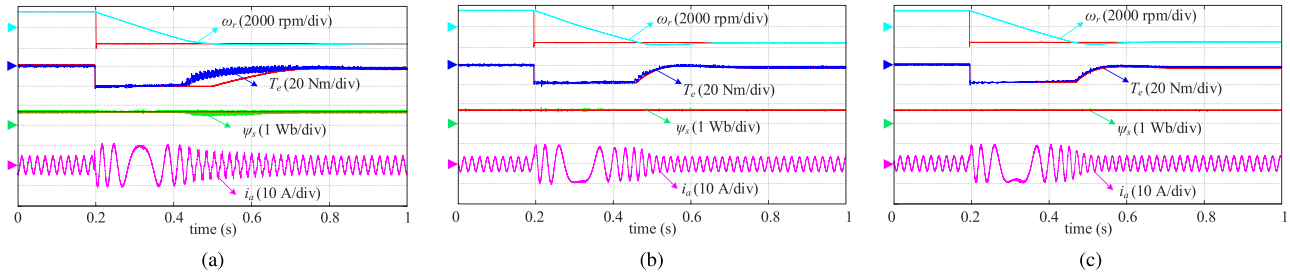

Fig. 19. Dynamic responses of speed reversion at 1500 rpm for (a) MPFC I, (b) MPFC II, and (c) MPFC III.

confirm that the proposed method outperforms DBC-SVM in terms of steady state performance especially at high speeds.

C. Dynamic Performance

The dynamic tests of the three control strategies are further carried out in this part. The pre-excitation is considered in these tests for the sake of providing sufficient torque during startup, and it will terminate once the stator flux reaches the given value, which equals to 98% of the reference in the tests. The waveforms are shown in Fig. 18, where the machine accelerates from standstill to rated speed of 1500 rpm after pre-excitation. The motor accelerates quickly to 1500 rpm without large starting current. Both MPFC II and MPFC III methods achieve accurate tracking of speed and torque in the transient process. On the contrary, the torque in MPFC I cannot track the reference value accurately during the dynamic process owing to the insufficient voltage caused by the fixed combination of a null vector and an active vector.

Fig. 19 shows the dynamic results of speed reversal operation at 1500 rpm. During the whole dynamic process, the stator flux is kept constant and the rotor speed follow the reference value quickly in each method. Again the relatively poor tracking ability of torque is observed in MPFC I. MPFC III has the shorter response time, lower current harmonics and torque ripples than MPFC I. The experimental results prove the satisfactory dynamic performance of the proposed strategies.

D. Comprehensive Comparison

At last, a comprehensive comparison of the three MPFC strategies is presented in Fig. 20 regarding to control performance in the full speed range. Obviously, although three control strategies all select two voltage vectors, the proposed MPFC II and MPFC III achieve lower current THD, torque ripples, and flux ripples owing to the extended control set of candidate VVs. By virtue of dynamic adjustment for applied vectors, MPFC III

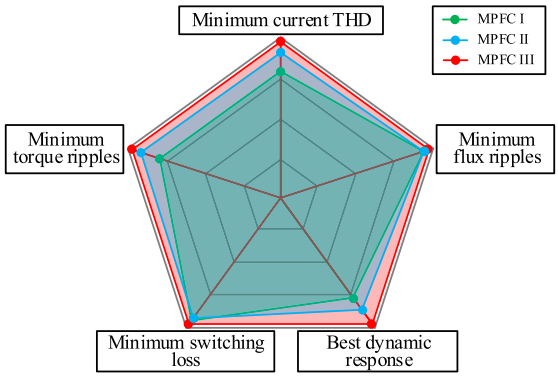

Fig. 20. Overall comparison results of each strategy.

can obtain the lowest average switching frequency than the other strategies. Meanwhile, MPFC III has faster dynamic response than MPFC I, and maintains the satisfactory control performance in the dynamic process. Hence, the proposed MPFC methods outperforms MPFC I in various aspects, which is more favorable for practical applications.

V. Conclusion

This article proposes an improved MPFC method based on duty cycle optimization schemes for IM drives. A symmetric two-vector combination is flexibly selected according to the minimum volt–second error, where the second vector is not limited to the null vector. Meanwhile, the duration of vectors is further optimized based on the principle of flux ripple minimization. As a result, the current harmonics and torque ripples are reduced significantly. Also, appropriate vector sequence adjustment ensures the low switching frequency. The proposed scheme is experimentally verified on an IM drive platform. The comparative steady state and dynamic experimental results validate the effectiveness of the proposed methods.

References

[1] F. Abrahamsen, F. Blaabjerg, J. K. Pedersen, and P. B. Thoegersen, "Efficiency-optimized control of medium-size induction motor drives," *IEEE Trans. Ind. Appl.*, vol. 37, no. 6, pp. 1761–1767, Nov./Dec. 2001.

[2] G. Mirzaeva and Y. Mo, "Model predictive control for industrial drive applications," *IEEE Trans. Ind. Appl.*, vol. 59, no. 6, pp. 7897–7907, Nov./Dec. 2023.

[3] J. Rodriguez et al., "Latest advances of model predictive control in electrical drives-Part I: Basic concepts and advanced strategies," *IEEE Trans. Power Electron.*, vol. 37, no. 4, pp. 3927–3942, Apr. 2022.

[4] M. Narimani, B. Wu, V. Yaramasu, Z. Cheng, and N. R. Zargari, "Finite control-set model predictive control (FCS-MPC) of nested neutral point-clamped (NNPC) converter," *IEEE Trans. Power Electron.*, vol. 30, no. 12, pp. 7262–7269, Dec. 2015.

[5] Y. Zhang, H. Yang, and B. Xia, "Model-predictive control of induction motor drives: Torque control versus flux control," *IEEE Trans. Ind. Appl.*, vol. 52, no. 5, pp. 4050–4060, Sep./Oct. 2016.

[6] Z. Xue, S. Niu, and X. Li, "A simplified multivector-based model predictive current control for PMSM with enhanced performance," *IEEE Trans. Transport. Electrific.*, vol. 9, no. 3, pp. 4032–4044, Sep. 2023.

[7] D. Cao, Y. Zhang, L. Han, and Y. Wang, "Improved asymmetric double-vector model-predictive current control of power converters with current harmonic minimization and switching frequency reduction," *IEEE Trans. Power Electron.*, vol. 40, no. 2, pp. 2833–2846, Feb. 2025.

[8] J. Zhao, Y. Zhang, and X. Wang, "Model-free predictive current control of PMSM drives based on variable sequence space vector modulation using an ultra-local model," *IEEE Trans. Transport. Electrific.*, vol. 10, no. 2, pp. 3518–3528, Jun. 2024.

[9] J.-K. Kang and S.-K. Sul, "New direct torque control of induction motor for minimum torque ripple and constant switching frequency," *IEEE Trans. Ind. Appl.*, vol. 35, no. 5, pp. 1076–1082, Sep./Oct. 1999.

[10] M. L. Parvathy and V. K. Thippiripati, "An effective modulated predictive current control of PMSM drive with low complexity," *IEEE Trans. Emerg. Sel. Topics Power Electron.*, vol. 10, no. 4, pp. 4565–4575, Aug. 2022.

[11] Y. Zhang and H. Yang, "Model predictive torque control of induction motor drives with optimal duty cycle control," *IEEE Trans. Power Electron.*, vol. 29, no. 12, pp. 6593–6603, Dec. 2014.

[12] C. Hu et al., "A novel double-voltage-vector model-free predictive current control method for two-level voltage source inverters," *IEEE Trans. Ind. Electron.*, vol. 70, no. 6, pp. 5872–5884, Jun. 2023.

[13] N. Jin, M. Chen, L. Guo, Y. Li, and Y. Chen, "Double-vector model-free predictive control method for voltage source inverter with visualization analysis," *IEEE Trans. Ind. Electron.*, vol. 69, no. 10, pp. 10066–10078, Oct. 2022.

[14] Y. Zhang and H. Yang, "Two-vector-based model predictive torque control without weighting factors for induction motor drives," *IEEE Trans. Power Electron.*, vol. 31, no. 2, pp. 1381–1390, Feb. 2016.

[15] T. Liu, A. Chen, C. Qin, J. Chen, and X. Li, "Double vector model predictive control to reduce common-mode voltage without weighting factors for three-level inverters," *IEEE Trans. Ind. Electron.*, vol. 67, no. 10, pp. 8980–8990, Oct. 2020.

[16] S. G. Petkar and V. K. Thippiripati, "Effective multivector-operated predictive current control of PMSM drive with reduced torque and flux ripple," *IEEE Trans. Transport. Electrific.*, vol. 9, no. 2, pp. 2217–2227, Jun. 2023.

[17] M. Nemec, K. Drobnic, D. Nedeljkovic, and V. Ambrozic, "Direct current control of a synchronous machine in field coordinates," *IEEE Trans. Ind. Electron.*, vol. 56, no. 10, pp. 4052–4061, Oct. 2009.

[18] X. Zhang and B. Hou, "Double vectors model predictive torque control without weighting factor based on voltage tracking error," *IEEE Trans. Power Electron.*, vol. 33, no. 3, pp. 2368–2380, Mar. 2018.

[19] X. Li, S. Zhang, C. Zhang, Y. Zhou, X. Yuan, and Y. Dong, "Model predictive control with duty ratio modulation for open-winding PMSM drives with common DC bus," *IEEE Trans. Power Electron.*, vol. 38, no. 12, pp. 15287–15299, Dec. 2023.

[20] Y. Wang, Y. Zhang, H. Yang, and J. Rodriguez, "Variable-vector-based model predictive control with reduced current harmonic and controllable switching frequency for PMSM drives," *IEEE Trans. Power Electron.*, vol. 39, no. 12, pp. 16429–16441, Dec. 2024.

[21] Y. Zhang, Y. Bai, and H. Yang, "A universal multiple-vector-based model predictive control of induction motor drives," *IEEE Trans. Power Electron.*, vol. 33, no. 8, pp. 6957–6969, Aug. 2018.

[22] K.-K. Shyu, J.-K. Lin, V.-T. Pham, M.-J. Yang, and T.-W. Wang, "Global minimum torque ripple design for direct torque control of induction motor drives," *IEEE Trans. Ind. Electron.*, vol. 57, no. 9, pp. 3148–3156, Sep. 2010.

[23] J. Li, W. Song, B. Liu, J. Guo, Y. Wu, and Y. Li, "A comparative study of current harmonics and switching frequency with different pulse patterns in duty-cycle-based model predictive current control," *IEEE Trans. Ind. Electron.*, vol. 70, no. 11, pp. 10891–10901, Nov. 2023.

[24] Y. Zhang and H. Yang, "Generalized two-vector-based model-predictive torque control of induction motor drives," *IEEE Trans. Power Electron.*, vol. 30, no. 7, pp. 3818–3829, Jul. 2015.

[25] J. Holtz, "The representation of AC machine dynamics by complex signal flow graphs," *IEEE Trans. Ind. Electron.*, vol. 42, no. 3, pp. 263–271, Jun. 1995.

[26] Y. Zhang, Y. Bai, H. Yang, and B. Zhang, "Low switching frequency model predictive control of three-level inverter-fed IM drives with speed-sensorless and field-weakening operations," *IEEE Trans. Ind. Electron.*, vol. 66, no. 6, pp. 4262–4272, Jun. 2019.

[27] Y. Zhu, Y. Zhang, J. Kang, and X. Wang, "MotorAST: A low-cost high-performance rapid control prototype platform for electric drives," in *Proc. IEEE Int. Conf. Predictive Control Elect. Drives Power Electron.*, 2023, pp. 1–6.

[28] P. Karamanakos and T. Geyer, "Guidelines for the design of finite control set model predictive controllers," *IEEE Trans. Power Electron.*, vol. 35, no. 7, pp. 7434–7450, Jul. 2020.

Chenhui Zhou was born in Rugao, Jiangsu, in 1998. She received the B.S. and M.S. degrees in electrical engineering from Nantong University, Nantong, China, in 2020 and 2023, respectively. She is currently working toward the Ph.D. degree in electrical engineering with North China Electric Power University, Beijing, China.

Her research focuses on the model predictive control of induction motor drives.

Yongchang Zhang (Fellow, IEEE) received the B.S. degree from Chongqing University, Chongqing, China, in 2004, and the Ph.D. degree from Tsinghua University, Beijing, China, in 2009, both in electrical engineering.

From 2009 to 2011, he was a Postdoctoral Fellow with the University of Technology Sydney, Sydney, NSW, Australia. He joined North China University of Technology in August 2011 as an Associate Professor, and was promoted to a Full Professor in January 2015. Since August 2021, he has been a Full Professor with North China Electric Power University, Beijing, China. He has authored or coauthored more than 100 technical papers in the area of motor drives, pulsewidth modulation, and ac/dc converters. His research focuses on model predictive control for power converters and motor drives.

Dr. Zhang is the Editor/Associate Editor for several international journals, such as IEEE JOURNAL OF EMERGING AND SELECTED TOPICS IN POWER ELECTRONICS, IEEE TRANSACTIONS ON ENERGY CONVERSION, and IEEE TRANSACTIONS ON INDUSTRY APPLICATIONS. He was the Technical Program Co-Chair of 5th/6th/7th IEEE International Conference on Predictive Control of Electrical Drives and Power Electronics. He is a Fellow of the Institute of Engineering and Technology.

Haitao Yang (Member, IEEE) received the B.S. degree from the Hefei University of Technology, Hefei, China, in 2009, the M.S. degree from the North China University of Technology, Beijing, China, in 2015, and the Ph.D. degree from the University of Technology Sydney, Sydney, NSW, Australia, in 2020, all in electrical engineering.

In 2020, he joined North China University of Technology, Beijing, China, as an Associate Professor. His research interests include control of motor drives and PWM converters.

Wenyue Zheng was born in 1998. She received the B.S. degree from Northeast Normal University, Changchun, China, in 2021, and the M.S. degree from North China Electric Power University, Beijing, China, in 2024, both in electrical engineering.

In July 2024, she joined State Grid Tangshan Power Supply Company, Tangshan, China. Her research focuses on the model predictive control of induction motor drives.